SCIENTIFIC REPORTS

natureresearch

OPEN

Synthesis of MgAC-Fe$_3$O$_4$/TiO$_2$ hybrid nanocomposites via sol-gel chemistry for water treatment by photo-Fenton and photocatalytic reactions

Vu Khac Hoang Bui[1], Duckshin Park[2], Tuyet Nhung Pham[1], Yejin An[3], Jin Seok Choi[4], Hyun Uk Lee[5], Oh-Hyeok Kwon[6], Ju-Young Moon[6], Ki-Tae Kim[3] & Young-Chul Lee[1]

MgAC-Fe$_3$O$_4$/TiO$_2$ hybrid nanocomposites were synthesized in different ratios of MgAC-Fe$_3$O$_4$ and TiO$_2$ precursor. X-ray diffraction (XRD), scanning electron microscopy (SEM), transmission electron microscopy (TEM), X-ray fluorescence spectrometry (XRF), electron spin resonance spectrometry (ESR), Brunauer-Emmett-Teller (BET), photoluminescence (PL), and UV photoelectron spectroscopy (UPS) were used to characterize the nanocomposites. The increase of MgAC-Fe$_3$O$_4$, in the hybrid nanocomposites' core-shell structure, led to the decrease of anatase TiO$_2$ peaks, thus reducing the photo-Fenton and photocatalytic activities. According to the obtained data, MgAC-Fe$_3$O$_4$ [0.05 g]/TiO$_2$ showed the best photo-Fenton and photocatalytic activities, having removed ~93% of MB (photo-Fenton reaction) and ~80% of phenol (photocatalytic reaction) after 20 and 80 mins, respectively. On the pilot scale (30 L), MgAC-Fe$_3$O$_4$ [0.05 g]/TiO$_2$ was completely removed after 27 and 30 hours by the photo-Fenton and photocatalytic activities, respectively. The synergistic effect gained from the combined photo-Fenton and photocatalytic activities of Fe$_3$O$_4$ and TiO$_2$, respectively, was credited for the performances of the MgAC-Fe$_3$O$_4$/TiO$_2$ hybrid nanocomposites.

Advanced oxidation processes (AOPs) including O$_3$/H$_2$O$_2$, UV/O$_3$, UV/H$_2$O$_2$, H$_2$O$_2$/Fe^{2+} and UV/TiO$_2$ have been utilized for removal of toxic organic compounds in water/waste water, air, and soil. AOPs produce hydroxyl radicals that contain powerful oxidants capable of oxidizing various organic compounds with one or many double bonds[1]. Recently, the potential of photocatalytic materials has been extended to other applications such as photo-corrosion inhibition, solar water splitting by combined with different materials[2–4]. Among AOPs materials, photocatalysis with TiO$_2$ nanoparticles (NPs) under UV/Visible light has attracted keen interest from the time of its first discovery by Frank and Bard[5], specifically due to its high oxidative power and chemical stability[6–8]. However, the limitation of TiO$_2$ NPs is their low quantum efficiency of photo-generated electron-hole pairs caused by a high and rapid recombination rate[9]. For example, Degussa P25, a well-known commercial product, can reduce only 14% of phenol at 365 nm in water[10]. Another major disadvantage of TiO$_2$ NPs is that they cannot be recycled post-reaction. Leakages of photocatalytic materials to aqueous solution, moreover, can lead to secondary pollution. These disadvantages can be overcome by coating TiO$_2$ NPs on the surfaces of magnetic components such as Fe$_3$O$_4$ NPs, which can be easily collected from solutions under magnetic fields[11].

[1]Department of BioNano Technology, Gachon University, 1342 Seongnamdaero, Sujeong-gu, Seongnam-si, Gyeonggi-do, 13120, Republic of Korea. [2]Korea Railroad Research Institute (KRRI), 176 Cheoldobakmulkwan-ro, Uiwang-si, 16150, Gyeonggi-do, Republic of Korea. [3]Department of Environmental Engineering, Seoul National University of Science and Technology, 232 Gongneung-ro, Nowon-gu, Seoul, 01811, Republic of Korea. [4]Analysis Center for Research Advancement, Korea Advanced Institute of Science and Technology (KAIST), Yuseong-gu, Daejeon, 34141, Republic of Korea. [5]Advanced Nano-surface Research Group, Korea Basic Science Institute (KBSI), Daejeon, 34133, Republic of Korea. [6]Department Beauty Design Management, Hansung University, 116 Samseongyoro-16gil, Seoul, 02876, Republic of Korea. Correspondence and requests for materials should be addressed to K.-T.K. (email: ktkim@seoultech.ac.kr) or Y.-C.L. (email: dreamdbs@gachon.ac.kr)
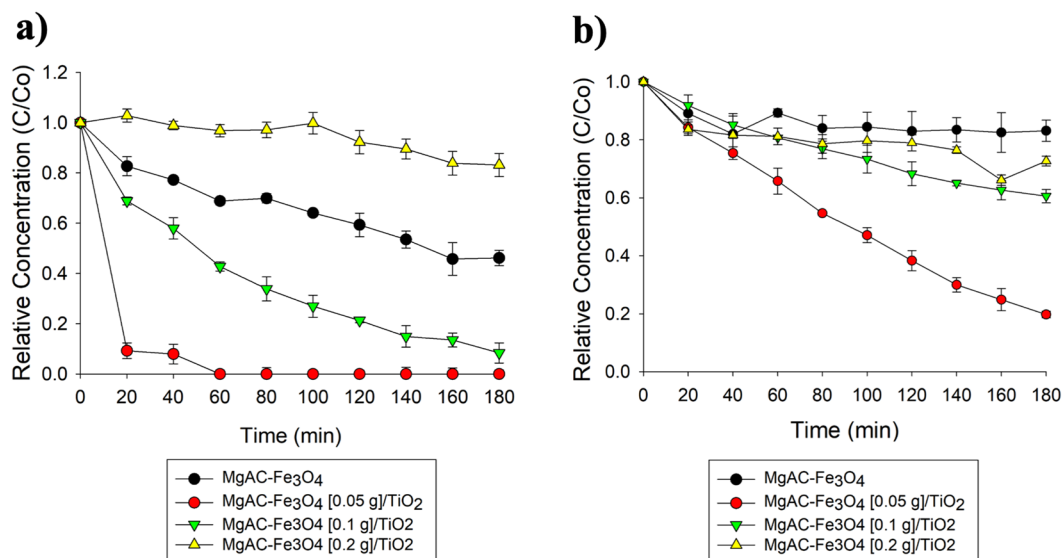
Figure 1. Photo-Fenton (MB, **a**) and photocatalytic performances (phenol, **b**) of MgAC-Fe₃O₄/TiO₂ hybrid nanocomposites on batch scale.

Fe₃O₄ NPs have attracted interest due to their considerable magnetic behavior and strong pin polarization[12]. Many methods of Fe₃O₄-TiO₂ composite synthesis, such as sol-gel, co-precipitation, hydrothermal, sonochemical, and templates routes, have been reported in the literature[12,13]. Incorporation of Fe₃O₄ NPs into a TiO₂ matrix can block NP aggregation and improve the durability of catalysts[14,15]. However, due to the small band gap of Fe₃O₄ NPs (0.1 eV), Fe₃O₄-TiO₂ composites will increase the rate of electron-hole pairs recombination, with the result that photocatalysis is usually unchanged or even diminished relative to pure TiO₂ NPs[12]. To overcome this problem, Zheng *et al.* demonstrated that special structures such as core-shell microspheres in Fe₃O₄-TiO₂ composites can delay the recombination of photo-induced electrons[12]; other researchers have used noble metal (Au or Ag) or rare elements (e.g. Eu) as electron traps to enhance electron-hole separation and facilitate electron excitation by creating a local hole in the electrical field[13,16,17]. In contrast, He *et al.*, after preparing Fe₃O₄-TiO₂ core-shell NPs, indicated that Fe³⁺ released from Fe₃O₄ can be doped into TiO₂ NPs to decrease electron-hole pair recombination and thus increase the photocatalytic performance of Fe₃O₄-TiO₂ core-shell NPs under visible light[18]. One remarkable report in this research field is that of Sun *et al.*, who found that a small number Fe₃O₄ NPs loaded onto TiO₂ NPs (Fe/TiO₂ ratio: 1/200) could enhance the degradation of organic dye (Reactive Brilliant Red X3B). They attributed the improved photocatalytic performance of Fe₃O₄-TiO₂ to the synergistic contribution of the photocatalytic and Fenton reactions in the composite[19].

2-D materials have been attracted and extended their applications due to their unique properties[20]. Photocatalytic materials have also been developed based on 2-D materials such as graphene[21].

From its first introduction by Mann *et al.*, magnesium aminoclay (MgAC), which is also another types of 2-D materials, has attracted interest in its propylamine functionalities, structures, and high dispersity in water[22–24]. Use of MgAC's high adsorption utility for heavy metal and organic dye removal has been reported[25]. Besides being utilized as a single agent, MgAC has been conjugated with other materials for environmental-treatment purposes. For example, MgAC has been coated with nZVI for removal of perfluorinated compounds[26] and chromium[27].

In previous work, we conjugated MgAC with TiO₂ NPs and Fe₃O₄ NPs by different methods for environmental-treatment[28,29] and microalgae-harvesting purposes[30,31]. The presence of MgAC in composites was demonstrated to improve the photocatalytic behavior of pure TiO₂ NPs[28] as well as the photo-Fenton behavior of Fe₃O₄ NPs[29]. Based on these successful preliminary results, in the present study, we synthesized MgAC-Fe₃O₄/TiO₂ hybrid composites in order to exploit the advantages of both Fe₃O₄ and TiO₂ in environmental-treatment applications.

Results and Discussion

Photo-Fenton performances of MgAC-Fe₃O₄/TiO₂ hybrid nanocomposites on batch scale.

Among different MgAC-Fe₃O₄/TiO₂ hybrid nanocomposites on the batch scale, the MgAC-Fe₃O₄ [0.05 g]/TiO₂ sample showed the best photo-Fenton performance, more than ~93% of MB having been removed after 20 min at a constant rate of ~0.1175 min⁻¹; this was ~10 and ~100 times higher than the performances of MgAC-Fe₃O₄ [0.1 g]/TiO₂ and MgAC-Fe₃O₄ [0.2 g]/TiO₂, which removed ~92 and ~17% of MB from aqueous solution after 180 min of reaction, respectively (Fig. 1a and Table 1).

We chose the MgAC-Fe₃O₄ [0.05 g]/TiO₂ sample to investigate the photo-Fenton performance when inhibition agents such as humic acid (HA), SO_4^{2-}, and HCO_3^- existed in the aqueous solution. Among these three inhibition agents, SO_4^{2-} and HCO_3^- had stronger inhibitory effects on the photo-Fenton reactions of the hybrid samples than HA, especially when these anionic and organic substances were presence at high concentrations in

Sample	Photo-Fenton constant rate against MB 10 ppm (min^{-1})	Photocatalytic constant rate against phenol 5 ppm (min^{-1})
MgAC-Fe$_3$O$_4$ [0.05 g]/TiO$_2$	**0.1175**	**0.0039**
MgAC-Fe$_3$O$_4$ [0.1 g]/TiO$_2$	0.0130	0.0012
MgAC-Fe$_3$O$_4$ [0.2 g]/TiO$_2$	0.0011	0.0006

Table 1. Degradation rates of MgAC-Fe$_3$O$_4$/TiO$_2$ hybrid nanocomposites by photo-Fenton and photocatalytic reaction on batch scale.
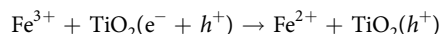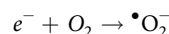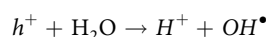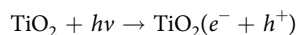
water (Fig. S2). The presence of HA, SO$_4^{2-}$, and HCO$_3^-$ can limit the photo-Fenton reaction of hybrid samples by reacting with generated reactive oxygen species (ROS)[32].

Photocatalytic performances of MgAC-Fe$_3$O$_4$/TiO$_2$ hybrid nanocomposites on batch scale. Instead of MB, we chose phenol to investigate the photocatalytic performances of the MgAC-Fe$_3$O$_4$/TiO$_2$ hybrid nanocomposites on the batch scale. Phenol is widely utilized in wastewater treatment within various industrial fields such as resins, petrochemicals, paints, textiles, oil refineries, foods, photographic chemicals, anti-oxidants and flavoring agents[33]. Phenol is a highly toxic pollutant that can cause environmental degradation and serious health problems in humans.

Among the samples, MgAC-Fe$_3$O$_4$ [0.05 g]/TiO$_2$ showed the best photocatalytic activity, ~80% of phenol having been removed after 180 min at a constant rate of 0.0039 min^{-1}; MgAC-Fe$_3$O$_4$ [0.1 g]/TiO$_2$ and MgAC-Fe$_3$O$_4$ [0.2 g]/TiO$_2$, by comparison, had removed only 40 and 27% of phenol, respectively (Fig. 1b and Table 1). The photocatalytic activities of the MgAC-Fe$_3$O$_4$/TiO$_2$ hybrid nanocomposites were attributed to the synergistic contributions of the photocatalytic and Fenton reactions in the hybrid nanocomposites[19]. In previous studies, Sun et al. indicated that increased Fe$_3$O$_4$ NP number could lead to decreased photocatalytic activity. Excess loading of Fe$_3$O$_4$ NPs promotes cluster aggregation, reduces O$_2$ adsorption, and thereby decreases the efficiency of interfacial charge transfer for pollutant degradation[19].

After 5 times recycle, the MgAC-Fe$_3$O$_4$ [0.05 g]/TiO$_2$ sample still remained ~80% of its initial removal efficiencies against phenol (Fig. S3). The deactivation of MgAC-Fe$_3$O$_4$ [0.05 g]/TiO$_2$ could be explained by the accumulation of phenol intermediate products on actives sites of hybrid nanocomposites[34]. The presence of these intermediate products in the reactor after stopping photocatalytic reaction could be supported by results of TOC below[35]. The hybrid nanocomposites could not be regenerated by using simple washing methods[34]. In the future works, the more suitable regeneration methods should be considered to improve the recycling performances.

Photo-fenton and photocatalytic mechanisms. The photocatalytic mechanism of MgAC-Fe$_3$O$_4$/TiO$_2$ was attributed to the presence of anatase TiO$_2$ in the samples, as follows:

$$TiO_2 + h\nu \rightarrow TiO_2(e^- + h^+)$$

$$h^+ + H_2O \rightarrow H^+ + OH^\bullet$$

$$h^+ + OH^- \rightarrow OH^\bullet$$

$$e^- + O_2 \rightarrow {}^\bullet O_2^-$$

$$Fe^{3+} + TiO_2(e^- + h^+) \rightarrow Fe^{2+} + TiO_2(h^+)$$

OH$^\bullet$ and $^\bullet$O$_2^-$, which are produced through the above chain reactions, will degrade pollutant molecules via oxidation and a reduction reaction process, respectively. To investigate the contribution of these ROS to the photocatalytic activity of MgAC-Fe$_3$O$_4$/TiO$_2$, different scavengers have been used: isopropanol for ●OH, methanol for both h$^+$ and ●OH, and p-benzoquinone for $^\bullet$O$_2^-$ [36,37]. In our system, highly reactive ●OH was the main actor in the degradation of the pollutant materials, rather than the valence band h$^+$ and the conductive band e$^-$ (Fig. S4)[36].

On the other hand, the photo-Fenton activities of the MgAC-Fe$_3$O$_4$/TiO$_2$ hybrid nanocomposites were extremely high, due to the presence of H$_2$O$_2$ in the reaction:

$$Fe^{2+} + H_2O_2 \rightarrow {}^\bullet OH + Fe^{3+} + OH^-$$

$$H_2O_2 + h\nu \rightarrow {}^\bullet OH$$
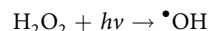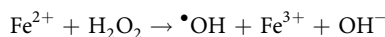
As noted just above, pollutants are degraded mainly by ●OH, which is generated in a photo-Fenton-like process: direct photolysis of H$_2$O$_2$, and photocatalytic oxidation of adsorbed H$_2$O through holes in the valence band of the TiO$_2$ surface. Additionally, photo-induced electrons generated from TiO$_2$ can cause reduction of Fe^{3+} to Fe^{2+} [38]. The photocatalytic and photo-Fenton activities of MgAC-Fe$_3$O$_4$/TiO$_2$ hybrid nanocomposites can be additionally supported by the presence of MgAC, which, with its high adsorption utility, can bring reactants to the surfaces of photo-Fenton agents[24,25].
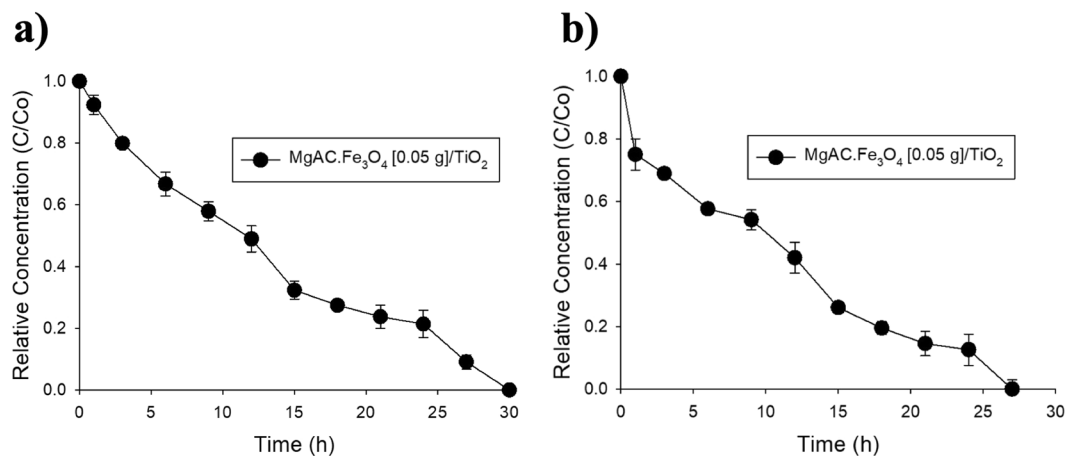
Figure 2. (**a**) Photocatalytic and (**b**) photo-Fenton performances of MgAC-Fe$_3$O$_4$ [0.05 g]/TiO$_2$ hybrid nanocomposites on pilot scale.

MgAC-Fe$_3$O$_4$ [0.05 g]/TiO$_2$	Constant rate (h^{-1})
Photocatalytic	0.0032
Photo-Fenton	0.0036

Table 2. Phenol-degradation rates of MgAC-Fe$_3$O$_4$/TiO$_2$ hybrid nanocomposites by photocatalytic and photo-Fenton reaction on pilot scale.

Photoluminescence spectra could be used to explain the photocatalytic mechanism[39]. From photoluminescence spectra (Fig. S5), it is clearly seen that, due to the presence of TiO$_2$ in the hybrid composites, the separated electron and holes were kept longer in excited state than original MgAC-Fe$_3$O$_4$ samples[40,41]. These results also were used to support the photocatalytic mechanisms of MgAC-Fe$_3$O$_4$/TiO$_2$ hybrid nanocomposites. In addition, MgAC-Fe$_3$O$_4$ [0.05 g]/TiO$_2$ have the lowest photoluminescence intensity.

Preliminary evaluation of photocatalytic and photo-Fenton performances of MgAC-Fe$_3$O$_4$/TiO$_2$ hybrid nanocomposites on pilot scale. The photocatalytic activities of TiO$_2$ NP materials have been widely investigated on the batch scale. However, for the purposes of industrial application, these materials need to be up-scaled to pilot-scale reactors. There are a variety of pilot reactors that have been introduced in the literature[26,27]. In this study, we used a design of pilot reactor that has been introduced in previous reports[28,29]. The design and photos of the pilot reactor are presented in Fig. S6.

Based on the batch-scale results discussed above, MgAC-Fe$_3$O$_4$ [0.05 g]/TiO$_2$ was mass produced for testing of photocatalytic and photo-Fenton performances on the pilot scale. For photocatalytic performance testing, 30 g of MgAC-Fe$_3$O$_4$ [0.05 g]/TiO$_2$ was added to the 30 L pilot reactor to obtain a dosage of 1 g/L (similarly to the batch-scale study). After 30 hours, phenol had been nearly completely removed from the aqueous solution at a constant rate of 0.032 (h^{-1}) (Fig. 2a and Table 2). The extended reaction time might be attributable to the heaviness of the materials, which is quickly self-precipitated. However, this phenomenon makes MgAC-Fe$_3$O$_4$ [0.05 g]/TiO$_2$ easily recoverable after the reaction. In this study, ~80% of the materials was recovered from the reactor by simply stopping the reactor and allowing self-precipitation to occur for 24 hours without any external force (Fig. S7). To shorten the reaction time, we added 50 mL of H$_2$O$_2$ to obtain ~15 ppm peroxide in the reactor while reducing the dosage of MgAC-Fe$_3$O$_4$ [0.05 g]/TiO$_2$ from 1 g/L to 0.5 g/L. Under this photo-Fenton condition, phenol was completely removed after 27 hours at a constant rate of increase to 0.036 (h^{-1}) (Fig. 2b and Table 2). It should be noted that in this paper, we present just the preliminary results; the optimal concentrations of photocatalytic materials and H$_2$O$_2$ should be discussed in future work investigating the effect of tap water on degradation rate. There is also a requirement for continual reactor upgrading to prevent quick sedimentation in the photocatalytic reaction and, thereby, improve the performance of MgAC-Fe$_3$O$_4$ [0.05 g]/TiO$_2$ on the pilot scale.

For phenol of 500 ppm, after 48 h exposure, the LC$_{50}$ was 6.39 mg/L (5.36–7.53, 95% CI). At the concentrations of 0, 2.5, 5, 7.5, 10, and 20 ppm, the mortality rates were 0, 15, 20, 50, 80, and 100%, respectively (Fig. S1b). Meanwhile, the treated samples showed a mortality rate of ~10% (Fig. S1c). We suspected that the remnant toxicity had come from the leakage of Fe^{3+} ions from the hybrid nanocomposites or the phenol intermediate products after the reactions. So, we conducted both ICP and TOC experiments to investigate the reason behind the toxicity of the treated samples. The ICP results showed that the leakage of iron ions after stoppage of the reaction was negligible (~60 ppb after treatment, lower than the standard 300 ppb for drinking water according to the WHO)[42]. However, the TOC experiments showed that the organic carbon concentration was still very high after the reaction (~50–55%); thus, the toxicity could be attributed to the residual toxic phenol intermediate products (Fig. S8). Therefore, it is necessary to extend the reaction until intermediate products are completely removed, not to the phenol concentration of zero[36].
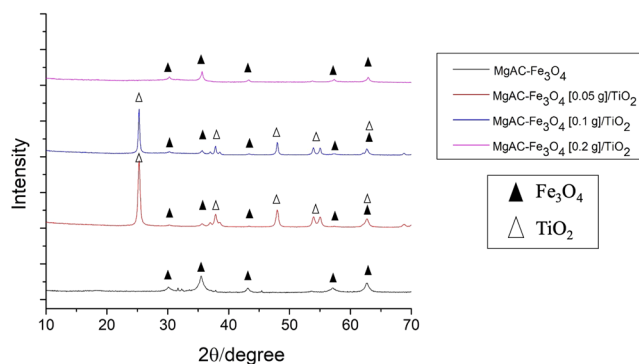
Figure 3. XRD patterns of MgAC-Fe$_3$O$_4$ and MgAC-Fe$_3$O$_4$/TiO$_2$ hybrid nanocomposites.

Characterization of hybrid nanocomposites.

The magnetic properties of the MgAC-Fe$_3$O$_4$/TiO$_2$ hybrid nanocomposites were preserved after the synthesis process (Fig. S9). The XRD pattern showed that, for the MgAC-Fe$_3$O$_4$ sample, the peaks at 29.98°, 35.5°, 42.9°, 56.7°, and 62° belonged respectively to (200), (311), (400), (511), and (440) of Fe$_3$O$_4$ magnetite (JCDS 00-021-1272; JCDS: Joint Committee on Power Diffraction Standard)[28]; meanwhile, for MgAC-Fe$_3$O$_4$ [0.05 g]/TiO$_2$ and MgAC-Fe$_3$O$_4$ [0.1 g]/TiO$_2$, besides the reduced MgAC-Fe$_3$O$_4$ peaks, there were additional peaks at 25.5°, 37.8°, 48.3°, 54.2°, and 62.8° belonging respectively to the (101), (004), (200), (105), and (204) planes of the anatase phase (JCDS 00-064-0863, Fig. 3)[28]. It was apparent that, for MgAC-Fe$_3$O$_4$ [0.1 g]/TiO$_2$, the high-intensity peaks of TiO$_2$ were reduced, whereas those of MgAC-Fe$_3$O$_4$ [0.2 g]/TiO$_2$ had totally disappeared. It could be concluded that the excess MgAC-Fe$_3$O$_4$ loading inhibited the growth of anatase TiO$_2$ in the hybrid nanocomposites. XRD was double checked by conducting two measurement to confirm the phenomena (Fig. S10). These results were similar with Sun *et al.*[19]. Also, the XPS analysis showed that, for MgAC-Fe$_3$O$_4$ [0.05 g]/TiO$_2$, besides the peaks at ~532, ~285, ~102, and ~52 eV belonging respectively to O 1s, C1s, Si 2p, and Mg 2p (Fig. S11a)[27,43], there were additional peaks at ~463 eV and ~457 eV that were attributed to the Ti 2p$_{1/2}$ and Ti 2p$_{3/2}$ of Ti^{4+} states of stoichiometric TiO$_2$, respectively (Fig. S11b)[44]. The Fe 2p$_{1/2}$ and Fe 2p$_{3/2}$ peaks of Fe$_3$O$_4$ existed at ~723.9 and ~710.2 eV, respectively (Fig. S11c)[45].

According to the SEM results, MgAC-Fe$_3$O$_4$ [0.05 g]/TiO$_2$ had an aggregated form, with a diameter ranging between 32.82 and 201.80 nm (Fig. 4a). The morphology of MgAC-Fe$_3$O$_4$ [0.05 g]/TiO$_2$ was further investigated by TEM and energy-dispersive X-ray mapping analysis (EDX). In the XRD, TEM, and EDX results, where MgAC-Fe$_3$O$_4$ was uniformly distributed in the TiO$_2$ matrix, MgAC-Fe$_3$O$_4$/TiO$_2$ showed a core-shell-like structure, MgAC-Fe$_3$O$_4$ playing the role as the core material and TiO$_2$ that of the out-layer material (Fig. 4b,c). Lattice fringe spacing of 0.253 nm, belonging to the (311) plane of the Fe$_3$O$_4$ NPs, and 0.355 nm of TiO$_2$ NPs in HR-TEM image confirmed the presence of these particles in the hybrid nanocomposites (Fig. 4d)[46,47]. From the XRF analysis results, the ratios between Fe$_3$O$_4$ and TiO$_2$ were ~1:12, 1:5.5, and 1:3.5 for MgAC-Fe$_3$O$_4$ [0.05 g]/TiO$_2$, MgAC-Fe$_3$O$_4$ [0.1 g]/TiO$_2$, and MgAC-Fe$_3$O$_4$ [0.2 g]/TiO$_2$, respectively (Table S1). XRF and XRD confirmed the effects of MgAC-Fe$_3$O$_4$ loading on the photocatalytic activities of the MgAC-Fe$_3$O$_4$/TiO$_2$ hybrid nanocomposites. Sun (2018) indicated that a ratio between Fe and TiO$_2$ of 1:200 could enhance the degradation of organic dye, increase the loading amount of Fe$_3$O$_4$ and, thus, decrease the photocalytic activity[19]. The amounts of MgO and SiO in the XRF analysis and of Mg, Si in the EDX mapping analysis were attributed to the presence of amorphous MgAC in the hybrid nanocomposites (Fig. 5c and Table S1).

As for the ESR spectrum, the two main signals at ~2.0 and ~4.3 could be assigned to different Fe(III) sites[48]. The broad signal at ~2.0 could be assigned to the interaction between iron (octahedral sites) and MgAC. This band could belong to the chain -O-Si-O-Fe-O-Si-O- from the reaction between the MgAC and Fe$_3$O$_4$ NPs[49]. The second signal at g ~4.3 corresponded to the strongly orthorhombic sites located on the surface or to the isolated Fe(III) ions dispersed in the silica matrix[50]. Additionally, the symmetric broad band at g ~2.0 confirmed the ferromagnetic properties of the MgAC-Fe$_3$O$_4$/TiO$_2$ hybrid nanocomposites (Fig. S12)[49]. Based on the characteristic data, the suggested structure of MgAC-Fe$_3$O$_4$/TiO$_2$ is provided in Fig. 5. In the synthesis of MgAC-Fe$_3$O$_4$, the presence of amino groups in the layered MgAC structure makes for high dispersibility in water[25]. The formation of the NH$_3^+$ and –OH groups on the surfaces of Fe$_3$O$_4$ NPs helps them to connect through strong electrostatic interaction. When the calcine process was carried out, besides the decomposition of amine groups on the surface material, there was evident formation of new bond bridges such as (-Fe-O-C$_3$-Si-O-Mg-O-Si-O-C$_3$-) within the architecture. (-C$_3$-O-Si-Mg-O-Si-O-C$_3$-) bridges within MgAC, for example, are very stable under harsh conditions. The large-interface surface area between Fe$_3$O$_4$ and MgAC facilitates formation of new bridges between Fe$_3$O$_4$ and MgAC at high temperature. This formation of new bridges suggests possible coordination of the O elements with the carbon elements and replacement of the O atoms in the NH$_3$ groups[51]. Fe$_3$O$_4$ NPs are not easy to coat with TiO$_2$ NPs layers, and so the presence of SiO$_2$ could overcome this problem[52,53]. Moreover, the SiO$_2$ layer formed in hybrid NPs can make space for the adsorption of polluted materials[53,54]. For synthesis of MgAC-Fe$_3$O$_4$/TiO$_2$, adding TiO$_2$ to the surfaces of synthetic material not only leads to increased photocatalytic activity but also forms a stable inter-connection. We offered some great bridges at the interface of the TiO$_2$ NPs and Fe$_3$O$_4$, such as (-O-Ti-O-Fe-O-Si-O-Mg-O-Si-O-Fe-O-Ti-O-) or (-O-Ti-O-Si-O-Mg-O-Si-O-Ti-O-). Based on the synthetic condition, it was clearly seen that many O atoms existing on the material surface could have resulted in the development of these new bridges. Besides, Si atoms are more electronegative and less polarizable than Fe and Ti
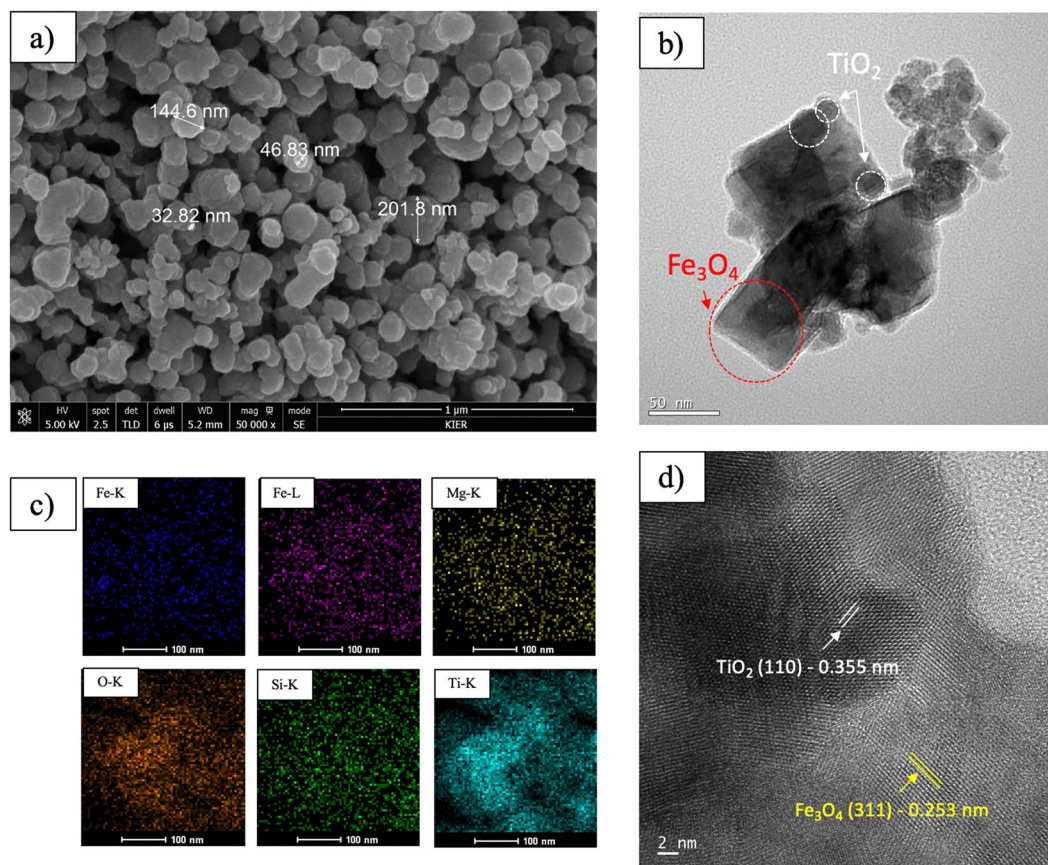
Figure 4. Morphology of MgAC-Fe$_3$O$_4$ [0.05 g]/TiO$_2$ hybrid nanocomposite. (**a**) SEM, (**b**) TEM, (**c**) EDX mapping analysis, and (**d**) HRTEM.
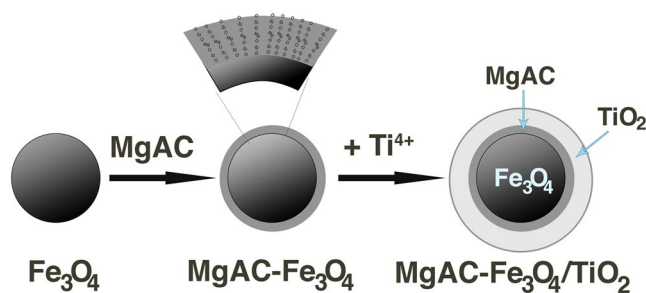

Figure 5. Scheme of process of MgAC-Fe$_3$O$_4$/TiO$_2$ synthesis.

atoms; the effective positive charge on Fe and Ti is increased, and the effective negative charge on O is decreased. In other words, the electron density around Fe and Ti atoms is decreased and the shielding effect is weakened, which results in increased binding energy.

From the obtained UPS spectra (Fig. S13), the work functions were calculated to 2.98, 1.87, 2.1, 1.95, and 1.56 eV for MgAC-Fe$_3$O$_4$, MgAC-Fe$_3$O$_4$ [0.05 g]/TiO$_2$, MgAC-Fe$_3$O$_4$ [0.1 g]/TiO$_2$, MgAC-Fe$_3$O$_4$ [0.2 g]/TiO$_2$, and MgAC-TiO$_2$, respectively (Table S2). It was noted that MgAC-TiO$_2$ was synthesized by using MgAC and titanium butoxide (TB) as precursors in ethanol media, as previously reported[28]. The decrease of work function could facilitate electron emission and narrow the energy band gap[55]. It was clearly seen that the work function of MgAC-Fe$_3$O$_4$ was lower than that of Fe$_3$O$_4$, which is around 3.7 eV in the literature[56]; this reduction of work function could be explained by the higher photo-Fenton activity of MgAC-Fe$_3$O$_4$ than that of commercial Fe$_3$O$_4$, as was demonstrated in a previous report[29]. The presence of TiO$_2$ on the surface of MgAC-Fe$_3$O$_4$ continued to decrease the work function, the lowest number belonging to MgAC-Fe$_3$O$_4$ [0.05 g]/TiO$_2$ (1.87 eV, optimal sample), which was yet larger than that of MgAC-TiO$_2$ (1.56 eV), which showed photocatalytic activation under visible light activation[28]. It could be concluded that, in general, the photocatalytic activity of the MgAC-Fe$_3$O$_4$/ TiO$_2$ hybrid nanocomposite is higher than that of MgAC-Fe$_3$O$_4$ (which has only photo-Fenton activity) but lower

Sample	BET surface area (m²/g)	Pore size (nm)	Pore volume (cm³/g)
MgAC-Fe$_3$O$_4$	34.790	3.639	0.0356
MgAC-Fe$_3$O$_4$ [0.05 g]/TiO$_2$	35.159	9.4163	0.0834
MgAC-Fe$_3$O$_4$ [0.1 g]/TiO$_2$	70.244	6.652	0.1280
MgAC-Fe$_3$O$_4$ [0.2 g]/TiO$_2$	31.44	10.629	0.0899
MgAC-TiO$_2$	87.822	7.595	0.1510

Table 3. BET surface areas, pore sizes and pore volumes of samples in this study.

than that of MgAC-TiO$_2$ (which also has photocatalytic activity under visible light irradiation). The advantages of MgAC-Fe$_3$O$_4$/TiO$_2$ relative to MgAC-TiO$_2$ come from its recycling utility. The difference of photocatalytic activity between the two might come from their respective synthesis processes and material structures. In the case of MgAC-TiO$_2$, nitrogen from the amino-functional groups of MgAC can be doped into the TiO$_2$ structure via a calcination process, thus inducing photocatalytic activity under visible light[57]. However, in the case of MgAC-Fe$_3$O$_4$/TiO$_2$ hybrid nanocomposites, the nitrogen element is removed by the process of the synthesis of MgAC-Fe$_3$O$_4$, as suggested above.

Additionally, the surface areas, pore sizes and pore volumes of the materials were investigated to characterize their surfaces. As can be seen in Table 3, the surface area, pore size and pore volume of the MgAC-Fe$_3$O$_4$ sample were the lowest (surface area: 34.790 m²/g; pore size: 3.639 nm; pore volume: 0.0356 cm³/g). In the literature, the adsorption capacity of Fe$_3$O$_4$ is lower than that of TiO$_2$[19]. In the present study, the MgAC-TiO$_2$ sample had the largest surface area, pore size and pore volume (surface area: 87.822 m²/g; pore size: 7.595 nm; pore volume: 0.1510 cm³/g). Surprisingly, for the MgAC-Fe$_3$O$_4$/TiO$_2$ hybrid nanocomposites, when TiO$_2$ existed on the surfaces of the MgAC-Fe$_3$O$_4$ particles, the surface area was not significantly changed (exception: MgAC-Fe$_3$O$_4$ [0.1 g]/TiO$_2$), whereas the pore size and pore volume were increased. For instance, for MgAC-Fe$_3$O$_4$ [0.05 g]/TiO$_2$ (the optimal sample), the pore size and pore volume were 9.4163 and 0.0834 cm³/g, 3 times larger than those of MgAC-Fe$_3$O$_4$. In general, even though the surface areas of MgAC-Fe$_3$O$_4$/TiO$_2$ hybrid nanocomposites are not significantly changed, their absorption capacities, via the increased pore sizes and volumes, are higher than that of MgAC-Fe$_3$O$_4$.

Discussion

MgAC-Fe$_3$O$_4$/TiO$_2$ samples were synthesized via sol-gel methods. The core-shell structure with Fe$_3$O$_4$ as the core component, SiO$_2$ as the middle layer and TiO$_2$ as outer layer was suggested. Based on the laboratory scale, the cost of MgAC-Fe$_3$O$_4$/TiO$_2$ materials has been calculated to around 1,479.80 USD/kg, similar to that of MgAC-TiO$_2$ (1,476.24 USD/kg; Table S3), due to its higher production efficiency (1 g MgAC can produce only 1.08 g of MgAC-TiO$_2$, whereas 1 g MgAC-Fe$_3$O$_4$ can produce 4.4 g of MgAC-Fe$_3$O$_4$ [0.05 g]/TiO$_2$). Another advantage of MgAC-Fe$_3$O$_4$/TiO$_2$ is its quick sedimentation, which enables ~80% of materials to be recovered after 24 hours of self-precipitation. Moreover, with their ferromagnetism was remained after the synthesis process, these hybrid nanocomposites show their recycling potential. However, the remnant toxicity of the treated sample against *Daphnia magna* indicated the presence of residual phenol intermediate products. The comparison of our study with some remarkable researches in the literature was briefly summarized in the Table 4.

For industrial-scale application purposes, the toxicity potential of MgAC-Fe$_3$O$_4$/TiO$_2$ as well as its photo-Fenton and photocatalytic mechanisms should be more thoroughly investigated. Additionally, it is necessary to find a way to induce the photocatalytic activity of such hybrid nanocomposites under visible light.

Methods

Materials. (3-aminopropyl)trielthoxysilane (APTES; ≥98%, 221.37 g/mol), iron (III) chloride hexahydrate (III) (FeCl$_3$·6H$_2$O; 97%) and titanium butoxide (TB; 97%) were obtained from Sigma-Aldrich (St. Louis, MO, USA). Magnesium chloride hexahydrate (MgCl$_2$·6H$_2$O; 98%) was purchased from Junsei Chemical (Tokyo, Japan). Ethanol (18 L, 95%) was acquired from Samchun Pure Chemicals (Pyungtack, Korea). NaOH (pellet, 97%) was purchased from Daejung Chemical & Metals (Siheung, Korea). Distilled-deionized water (DI; resistance: >18 mΩ) was employed in all of the experiments.

Synthesis of magnesium aminoclay (MgAC). For preparation of MgAC, 1.68 g of MgCl$_2$·6H$_2$O was dissolved in 40 mL of ethanol. Then, 2 mL of 3-aminopropyltrielthoxylane (APTES) was added and stirred for 8 hours to form a white suspension. The resultant suspension was then centrifuged and washed with ethanol (3 × 50 mL) before being dried at 40 °C and ground into powder[58].

Synthesis of magnesium aminoclay-iron oxide (MgAC-Fe$_3$O$_4$) nanocomposites. A total of 0.7 g of MgAC was mixed with 3 g of FeCl$_3$·6H$_2$O in 40 mL of DI water, to which mixture 10 mL of NaOH 10 M was added. The solution was stirred for 12 hours and then centrifuged and washed with DI water (3 × 50 mL) and dried at 60 °C to form a brown solid. The brown products were ground into powder and calcinated at 500 °C for 3 hours in a furnace (FU-100TG, Samheung Energy, Korea) under 4% H$_2$/Ar (flow rate: 0.15 L/min) to produce MgAC-Fe$_3$O$_4$ nanocomposites[29].

Synthesis of magnesium aminoclay-iron oxide/TiO$_2$ (MgAC-Fe$_3$O$_4$/TiO$_2$) hybrid nanocomposites. In order to prepare MgAC-Fe$_3$O$_4$/TiO$_2$ hybrid nanocomposites, respectively 0.05 g, 0.1 g and 0.2 g of

	Preparation Method	Obtained material	Remarkable results
He et al.[18]	Homogenous precipitation	Core-shell Fe_3O_4-TiO_2	● Obtained Fe_3O_4-TiO_2 is non-toxic ● Fe^{3+} could be doped into TiO_2 and activate the photocatalytic activation under visible light activation
Sun et al.[19]	One-step calcination	Magnetic Fe_3O_4-TiO_2	● The degradation of organic dye by Fe_3O_4-TiO_2 (Fe/TiO_2 ratio: 1/200) was enhanced compared to single Fe_3O_4 and TiO_2 ● The synergistic of Fe_3O_4 and TiO_2 could be attributed to the high photocatalytic activity
Zheng et al.[12]	Liquid phase deposition	Waxberry-like microsphere Fe_3O_4-TiO_2	● Diameter: ~500 nm ● Shell thickness: ~10–20 nm ● Remove 40% of MB (10 ppm) after 60 mins under Xenon lamp (300 W) ● Could be recycled after photocatalytic reaction
Stefan et al.[13]	Ultrasound assisted sol-gel	Fe_3O_4-TiO_2: Eu nanocomposite	● Increase of Eu doping decrease the formation of $FeTiO_3$ ● Large surface area and mesoporous strcuture ● Remove 85% of RhB (1.0×10^{-5} mol/L) dye after 3 h under visible light irradiation (400 W halogen lamp)
Alzahani[53]	Sol-gel	Core shell Fe_3O_4/SiO_2/TiO_2	● Under UV light, the photocatalytic performance was higher than commercial TiO_2
This study	**Sol-gel**	**MgAC-Fe_3O_4/TiO_2**	● **The synergistic of Fe_3O_4 and TiO_2 could be attributed to the performances of MgAC-Fe_3O_4/TiO_2** ● **Core-shell structure with Fe_3O_4 as core and TiO_2 at outer layer is suggested**. ● **However, the photocatalytic under visible light should be activated in the near future**

Table 4. The comparison of our study with some remarkable researches in the literature.

MgAC-Fe_3O_4 were mixed with 1 mL of TB in 40 mL EtOH, to each of which mixtures 0.25 µL of DI water was slowly added; the resultant solutions were denoted MgAC-Fe_3O_4 [0.05 g]/TiO_2, MgAC-Fe_3O_4 [0.1 g]/TiO_2, and MgAC-Fe_3O_4 [0.2 g]/TiO_2, respectively. Each solution was then stirred for at least 12 hours, washed with ethanol (3×50 mL) and dried to form a grey solid. The resultant products were then ground and consequently calcinated at 350 °C for 3 hours under air in a muffle furnace to produce MgAC-Fe_3O_4/TiO_2 hybrid nanocomposites[28].

Photo-fenton performances of MgAC-Fe_3O_4/TiO_2 hybrid nanocomposites on batch scale. A total of 0.1 g of MgAC-Fe_3O_4/TiO_2 hybrid nanocomposites was loaded into 100 mL of methylene blue (MB; Sigma-Aldrich, St. Louis, MO, USA) at a concentration of 10 ppm. After obtainment of equilibrium adsorption, 1 mL of H_2O_2 (35%) was added, and a 365 nm (24 W) UV light source was turned on. One (1) mL of treated water was withdrawn after an interval of 20 min, and the MB concentration was observed under UV-Vis spectroscopy (Cary 50-UV Vis Spectrophotometers, Varian Inc., USA) at a wavelength of 664 nm[28].

The degradation rate of the organic compounds was determined by the equation

$$-\frac{[C]}{dt} = k[C_o]$$

where C is the concentration of MB at time (t), C_o is the initial MB concentration, and k is the pseudo-first-order rate constant (min^{-1})[19].

Photocatalytic performances of MgAC-Fe_3O_4/TiO_2 hybrid nanocomposites on batch scale. For evaluation of the photocatalytic performances of MgAC-Fe_3O_4/TiO_2 hybrid nanocomposites, 0.1 g of MgAC-Fe_3O_4/TiO_2 hybrid nanocomposites was loaded into a petri dish of 100 mL of phenol at 5 ppm ($\geq$99%; Sigma-Aldrich, St. Louis, MO, USA). After obtainment of equilibrium adsorption, a 365 nm wavelength UV light source (~610 µW/cm²) was turned on. Interval samples were withdrawn after each 20 min, and the remaining organic compounds were detected by high-performance liquid chromatography (for phenol; HPLC, Waters Alliance 2695 Separations Module equipped with Waters 2487 Dual λ Absorbance Detector; Waters, Milford, MA, USA) under the mobile phase of water and acetonitrile in a ratio of 40:60 (v/v) with a flow rate of 1 mL/min[59]. For detection of phenol, UV absorption was performed at 270 nm.

The recycle usage experiments were conducted to check the stability of materials. After photocatalyst materials were separated from degraded solution, they were washed with DI water and ethanol, then dried in the oven at 60 °C for 12 hours. Then the materials is ready for another photocatalytic experiments. This method was repeated for 5 times[53].

Preliminary evaluation of photocatalytic and photo-Fenton performances of MgAC-Fe_3O_4/TiO_2 hybrid nanocomposites on pilot scale. The photocatalytic performances of the MgAC-Fe_3O_4/TiO_2 hybrid nanocomposites were tested using the systems introduced in a previous report[28]. Briefly, MgAC-Fe_3O_4/TiO_2 hybrid nanocomposites were loaded into a reactor (90 cm (width) $\times$ 30 cm (depth) $\times$ 60 cm (height)) containing 30 L of tap water contaminated with phenol at 3 ppm and stirred with 3 stirrers (GGM speed control motor, Korea) at 145 rpm. After obtainment of equilibrium adsorption, 18×365 nm wavelength UV lamps (light intensity: ~610 µW/cm², 65 cm $\times$ 3 cm) were turn on. After an interval of 3 hours, 40 mL of treated water was withdrawn, and the remaining concentration of phenol was determined by HPLC. For evaluation of the photo-Fenton

performances of the MgAC-Fe$_3$O$_4$/TiO$_2$ hybrid nanocomposites, H$_2$O$_2$ was supplied after obtainment of equilibrium adsorption.

For an ecotoxicity test, *Daphnia magna* was incubated in a 16 h light/8 h darkness cycle at 21 ± 1 °C with M4 medium prepared according to OECD Test Guideline 202 (OECD, 2014)[60]. The culture medium was replaced daily, and *Chlorella* was fed once a day. The *Daphnia* test was carried out according to OECD Test Guideline 202, and young daphanids aged less than 24 hours were collected and exposed to the test materials for 48 hours after *Chlorella* feeding for 2 hours. In the case of 500 ppm phenol feedstock, 5 daphanids were exposed to 25 mL of 0, 2.5, 5, 7.5, 10, and 20 ppm phenol to determine the LC$_{50}$ (Fig. S1a). Ecotoxicity tests of photo-Fenton- and photocatalytic-treated samples against *Daphnia magna* also were performed. The toxicity of the photo-Fenton and photocatalytic samples also were investigated, first, via inductive coupled plasma atomic emission spectroscopy (ICP-AES; Optima 7300 DV, Pelkin Elmer, USA) for leakage of iron ions and, second, via total organic carbon (TOC, Vario TOC Cube, Elementar, Germany) for the presence of intermediate products, after the reaction.

Characterization. The crystallography of the MgAC-Fe$_3$O$_4$/TiO$_2$ hybrid nanocomposites was examined using a Rigaku D/max-2500 (18 kW, Japan) incorporating a θ/θ goniometer equipped with a 40 kV, 30 mA CuKα radiation generator. The morphology of the MgAC-Fe$_3$O$_4$/TiO$_2$ hybrid nanocomposites was investigated by scanning electron microscopy (SEM; SEM-4700, Japan) and transmission electron microscopy (TEM; JEM-2100F, JEOL Ltd., USA). X-ray fluorescence spectrometry (XRF; MiniPal 2, PANanalytical, Almelo, Netherlands) was employed to identify the elemental compositions of as-prepared samples. The surface areas, pore sizes and pore volumes of the materials were investigated by Brunauer-Emmett-Teller (BET; Micromeritics ASAP 2010, USA)[25]. The photoluminescence (PL) spectra were obtained to investigate the electron-hole fate of the semiconductor (DUT-260, Core Bio System, Korea)[40]. The magnetic properties of the MgAC-Fe$_3$O$_4$/TiO$_2$ hybrid nanocomposites were examined by electron spin resonance spectrometry (ESR; EMXplus/ELEXYS E580, Bruker, USA).

Next, for investigation of the optical properties of the materials, UV photoelectron spectroscopy (UPS; Axis Ultra DLD, Japan) with He I line (21.2 eV) UV source was applied. The work functions of the materials were calculated by the equation

$$WF = h\nu - |E_{cutoff} - E_F|$$

where $h\nu$ is the incident energy (21.2 eV), E_{cutoff} is the secondary electron cutoff energy, and E_f is the Fermi energy[55].

Data Availability

The datasets generated and analysed during the current study are available from the corresponding author on reasonable request.

References

1. Daghir, R., Drogui, P. & Robert, D. Modified TiO$_2$ for enviromental photocatalytic application: a review. *Ind. Eng. Chem. Res.* **52**, 3581–3599 (2013).
2. Weng, B., Qi, M.-Y., Han, C., Tang, Z.-R. & Xu, Y.-J. Photocorrosion inhibition of semiconductor-based photocatalysts: basic principle, current development, and future perspective. *ACS Catal.* **9**, 4642–4687 (2019).
3. Li, Y.-B. *et al.* Cascade charge transfer mediated by *in situ* interface modulation toward solar hydrogen production. *J. Mater. Chem. A* **7**, 8938–8951 (2019).
4. Zheng, Z. *et al.* Plasmon-induced photoelectrochemical water oxidation enabled by *in situ* layer-by-layer construction of cascade charge transfer channel in multilayered photoanode. *J. Mater. Chem. A* **6**, 24686–24692 (2018).
5. Frank, S. N. & Bard, A. J. Heterogeneous photocatalytic oxidation of cyanide and sulfite in aqueous solutions at semiconductor powders. *J. Phys. Chem.* **81**, 1484–1488 (1977).
6. Kumar, S. G. & Rao, K. S. R. K. Comparison of modification strategies towards enhanced charge carrier separation and photocatalytic degradation activity of metal oxide semiconductors (TiO$_2$, WO$_3$ and ZnO). *Appl. Surf. Sci.* **391**, 124–148 (2017).
7. Low, J., Cheng, B. & Yu, J. Surface modification and enhanced photocatalytic CO$_2$ reduction performance of TiO$_2$: a review. *Appl. Surf. Sci.* **392**, 658–686 (2017).
8. Schneider, J. *et al.* Understanding TiO$_2$ photocatalysis: Mechanisms and materials. *Chem. Rev.* **114**, 9919–9986 (2014).
9. Huang, Q., Kang, F., Liu, H., Li, Q. & Xiao, X. Highly aligned Cu$_2$O/CuO/TiO$_2$ core/shell nanowire arrays as photocathodes for water photoelectrolysis. *J. Mater. Chem. A* **1**, 2418–2425 (2013).
10. Emeline, A. V., Zhang, X., Jin, M., Murakami, T. & Fujishima, A. Application of a "black body" like reactor for measurements of quantum yields of photochemical reactions in heterogeneous systems. *J. Phys. Chem. B* **110**, 7409–7413 (2006).
11. Zielińska-Jurek, A. *et al.* Magnetic semiconductor photocatalysts for the degradation of recalcitrant chemicals from flow back water. *J. Environ. Manage.* **195**, 157–165 (2017).
12. Zheng, J. *et al.* Direct liquid phase deposition fabrication of waxberry-like magnetic Fe$_3$O$_4$@TiO$_2$ core-shell microspheres. *Mater. Chem. Phys.* **181**, 391–396 (2016).
13. Stefan, M. *et al.* Magnetic recoverable Fe$_3$O$_4$-TiO$_2$: Eu composite nanoparticles with enhanced photocatalytic activity. *Appl. Surf. Sci.* **390**, 248–259 (2016).
14. Cheng, W., Tang, K., Qi, Y., Sheng, J. & Liu, Z. One-step synthesis of superparamagnetic monodisperse porous Fe$_3$O$_4$ hollow and core-shell spheres. *J. Mater. Chem.* **20**, 1799–1805 (2010).
15. Liu, Z., Bai, H. & Sun, D. D. Facile fabrication of porous chitosan/TiO$_2$/Fe$_3$O$_4$ microspheres with multifunction for water purifications. *New J. Chem.* **35**, 137–140 (2011).
16. Jia, X. *et al.* Facile synthesis and enhanced magnetic, photocatalytic properties of one-dimensional Ag@Fe$_3$O$_4$-TiO$_2$. *Appl. Surf. Sci.* **392**, 268–276 (2017).
17. Ma, J., Guo, S., Guo, X. & Ge, H. A mild synthetic route to Fe$_3$O$_4$@TiO$_2$-Au composites: preparation, characterization and photocatalytic activity. *Appl. Surf. Sci.* **353**, 1117–1125 (2015).
18. He, Q., Zhang, Z., Xiong, J., Xiong, Y. & Xiao, H. A novel biomaterial — Fe$_3$O$_4$: TiO$_2$ core-shell nano particle with magnetic performance and high visible light photocatalytic activity. *Opt. Mater.* **31**, 380–384 (2008).
19. Sun, Q., Hon, Y., Liu, Q. & Dong, L. Synergistic operation of photocatalytic degradation and Fenton process by magnetic Fe$_3$O$_4$ loaded TiO$_2$. *Appl. Surf. Sci.* **430**, 399–406 (2018).

20. Li, S.-H., Zhang, N., Xie, X., Luque, R. & Xu, Y.-J. Stress-transfer-induced *in situ* formation of ultrathin nickel phosphide nanosheets for efficient hydrogen evolution. *Angew. Chem.* **130**, 13266–13269 (2018).
21. Lu, K.-Q., Xin, X., Zhang, N., Tang, Z.-R. & Xu, Y.-J. Photoredox catalysis over graphene aerogel-supported composites. *J. Mater. Chem. A* **6**, 4590–4604 (2018).
22. Burkett, S. L., Press, A. & Mann, S. Synthesis, characterization and reactivity of layer inorganic-organic nanocomposites based on 2:1 trioctanhedral phyllosilicates. *Chem. Mater.* **9**, 1071–1073 (1997).
23. Mann, S. *et al.* Sol-gel synthesis of organized matter. *Chem. Mater.* **9**, 2300–2310 (1997).
24. Whilton, N. T., Burkett, S. L. & Mann, S. Hybrid lamellar nanocomposites based on organically functionalized magnesium phyllosilicate clays with interlayer reactivity. *J. Mater. Chem.* **8**, 1927–1932 (1998).
25. Bui, V. K. H., Park, D. & Lee, Y.-C. Aminoclays for biological and environmental applications: An updated review. *Chem. Eng. J.* **336**, 757–775 (2018).
26. Arvaniti, O. S. *et al.* Reductive degradation of perfluorinated compounds in water using Mg-aminoclay coated nanoscale zero valent iron. *Chem. Eng. J.* **262**, 133–139 (2015).
27. Wang, R., Jing, G., Zhou, X. & Lv, B. Removal of chromium (VI) from wastewater by Mg-aminoclay coated nanoscale zero-valent iron. *J. Water Process Eng.* **18**, 134–143 (2017).
28. Bui, V. K. H. *et al.* One-pot synthesis of magnesium aminoclay-titanium dioxide nanocomposites for improved photocatalytic performance. *J. Nanosci. Nanotech.* **18**, 6070–6074 (2018).
29. Bui, V. K. H., Pham, T. N. & Lee, Y.-C. One-pot synthesis of magnesium aminoclay-iron oxide nanocomposites for improved photo-Fenton catalytic performance. *J. Nanosci. Nanotech.* **19**, 1069–1073 (2019).
30. Lee, Y.-C. *et al.* Aminoclay-conjugated TiO$_2$ synthesis for simultaneous harvesting and wet-disruption of oleaginous *Chlorella* sp. *Chem. Eng. J.* **245**, 143–149 (2014).
31. Kim, B. *et al.* Magnesium aminoclay-Fe$_3$O$_4$ (MgAC-Fe$_3$O$_4$) hybrid composites for harvesting of mixed microalgae. *Energies* **11**, https://doi.org/10.3390/en11061359 (2018).
32. Qian, Y., Zhang, J., Zhang, Y., Chen, J. & Zhou, X. Degradation of 2,4-dichlorophenol by nanoscale calcium peroxide: Implication for groundwater remediation. *Sep. Purif. Technol.* **166**, 222–229 (2016).
33. Yu, L. *et al.* Degradation of phenol using Fe$_3$O$_4$-GO nanocomposite as a heterogeneous photo-Fenton catalyst. *Sep. Purif. Technol.* **171**, 80–87 (2016).
34. Cao, L. *et al.* Photocatalytic oxidation of toluene on nanoscale TiO$_2$ catalysts: studies of deactivation and regeneration. *J. Catal.* **196**, 253–261 (2000).
35. Mahvi, A. H., Maleki, A., Alimohamadi, M. & Ghasri, A. Photo-oxidation of phenol in aqueous solution: toxicity of intermediates. *Korean J. Chem Eng.* **24**, 79–82 (2007).
36. An, T. *et al.* Photocatalytic degradation and mineralization mechanism and toxicity assessment of antivirus drug acyclovir: Experimental and theoretical studies. *Appl. Catal. B-Environ.* **164**, 279–285 (2015).
37. Talukdar, S. & Dutta, R. K. A mechanistic approach for superoxide radicals and singlet oxygen mediated enhanced photocatalytic dye degradation by selenium doped ZnS nanoparticles. *RSC Adv.* **6**, 928–936 (2016).
38. Du, D., Shi, W., Wang, L. & Zhang, J. Yolk-shell structured Fe$_3$O$_4$@void@TiO$_2$ as a photo-Fenton-like catalyst for the extremely efficient elimination of tetracycline. *Appl. Catal. B-Environ.* **200**, 484–492 (2017).
39. Weng, B., Lu, K.-Q., Tang, Z., Chen, H. M. & Xu, Y.-J. Stabilizing ultrasmall Au clusters for enhanced photoredox catalysis. *Nat. Commun.* **9**, 1543 (2018).
40. Chen, F. *et al.* Fabrication of Fe$_3$O$_4$@SiO$_2$@TiO$_2$ nanoparticles supported by graphene oxide sheets for the repeated adsorption and photocatalytic degradation of rhodamine B under UV irradiation. *Dalton T.* **36**, 13537–13544 (2014).
41. Zhang, L. *et al.* Preparation of magnetic Fe$_3$O$_4$/TiO$_2$/Ag composite microspheres with enhanced photocatalytic activity. *Solid State Sci.* **52**, 42–48 (2016).
42. World Health Organization. In *Guidelines for drinking-water quality* (Geneva, 1996).
43. Wang, S. G. *et al.* Evidence for FeO formation at the Fe/MgO interface in epitaxial TMR structure by X-ray photoelectron spectroscopy. *J. Magn. Magn. Mater.* **310**, 1935–1936 (2007).
44. Giorgi, L. *et al.* Electrochemical synthesis of self-organized TiO$_2$ crytalline nanotubes without annealing. *Nanotechnology* **29**, 095604 (2018).
45. Han, F., Ma, L., Sun, Q., Lei, C. & Lu, A. Rationally designed carbon-coated Fe$_3$O$_4$ coaxial nanotubes with hierarchical porosity as high-rate anodes for lithium ion batteries. *Nano Res.* **7**, 1706–1717 (2014).
46. Li, G., Li, R. & Zhou, W. A wire-shaped supercapacitor in micrometer size based on Fe$_3$O$_4$ nanosheet arrays on Fe wire. *Nano-Micro Lett.* **9** (2017).
47. Chimupala, Y. *et al.* Synthesis and characterization of mixed phase anatase TiO$_2$ and sodium doped TiO$_2$(B) thin fims by low pressure chemical vapour deposition (LPCVD). *RCS Adv.* **4**, 48507–48517 (2014).
48. Tanaka, K., Kamiya, K., Matsuoka, M. & Yoko, T. ESR study of a sol-gel-derived amorphous Fe$_2$O$_3$-SiO$_2$ system. *J. Non-Cryst. Solids* **94**, 365–373 (1987).
49. Jitianu, A., Crisan, M., Meghea, A., Rau, I. & Zaharescu, M. Influence of the silica based matrix on the formation of iron oxide nanoparticles in the Fe$_2$O$_3$-SiO$_2$ system, obtained by sol-gel method. *J. Mater. Chem.* **12**, 1401–1407 (2002).
50. Cannas, C., Gatteschi, D., Musinu, A., Piccaluga, G. & Sangregorio, C. Structural and Magnetic Properties of Fe$_2$O$_3$ nanoparticles dispersed over a silica matrix. *J. Phys. Chem. B* **102**, 7721–7726 (1998).
51. Zubir, N. A., Yacou, C., Motuzas, J., Zhang, X. & Diniz da Costa, J. C. Structural and functional investigation of graphene oxide–Fe3O4 nanocomposites for the heterogeneous Fenton-like reaction. *Sci. Rep.* **4**, 4594 (2014).
52. De Matteis, L. *et al.* Influence of a silica interlayer on the structural and magnetic properties of sol–gel TiO$_2$-coated magnetic nanoparticles. *Langmuir* **30**, 5238–5247 (2014).
53. Alzahrani, E. Photodegradation of binary azo dyes using core-shell Fe$_3$O$_4$/SiO$_2$/TiO$_2$ nanospheres. *Am. J. Analyt. Chem.* **08**, 95–115 (2017).
54. Wang, R., Wang, X., Xi, X., Hu, R. & Jiang, G. Preparation and photocatalytic activity of magnetic Fe$_3$O$_4$/SiO$_2$/TiO$_2$. composites. *Adv. Mater. Sci. Eng.* **2012**, 8 (2012).
55. Lee, S. C. *et al.* Hierarchically three-dimensional (3D) nanotubular sea urchin-shaped iron oxide and its application in heavy metal removal and solar-induced photocatalytic degradation. *J. Hazard. Mater.* **354**, 283–292 (2018).
56. Liu, F. *et al.* Fabrication of vertically aligned single-crystalline boron nanowire arrays and investigation of their field-emission behavior. *Adv. Mater.* **20**, 2609–2615 (2008).
57. Wu, W., Xiao, X., Zhang, S., Ren, F. & Jiang, C. Facile method to synthesize magnetic iron oxides/TiO$_2$ hybrid nanoparticles and their photodegradation application of methylene blue. *Nanoscale Res. Lett.* **6**, 533 (2011).
58. Patil, A. J., Li, M., Dujardin, E. & Mann, S. Novel bioinorganic nanostructures based on mesolamellar intercalation or single-molecule wrapping of DNA using organoclay building blocks. *Nano Lett.* **7**, 2660–2665 (2007).
59. Liu, Z. *et al.* Highly ordered TiO$_2$ nanotube arrays with controllable length for photoelectrocatalytic degradation of phenol. *J. Phys. Chem. C* **112**, 253–259 (2008).
60. Organization for Economic Co-operation and Development (2004).

Acknowledgements

Author Contributions

Vu Khac Hoang Bui and Young-Chul Lee designed the study, prepared materials, conducted the experiment and wrote the manuscript mainly. Vu Khac Hoang Bui and Tuyet Nhung Pham analyzed the structure of materials. Yejin An and Ki-Tae Kim conducted the ecotoxicity experiments. Hyun Uk Lee helped to explain ESR results. Young-Chul Lee and Ki-Tae Kim are corresponding authors of this work. Duckshin Park, Jin Seok Choi, Oh-Hyeok Kwon and Ju-Young Moon contributed comments on the manuscript before submission.

Additional Information

Supplementary information accompanies this paper at https://doi.org/10.1038/s41598-019-48398-5.

Competing Interests: The authors declare no competing interests.

Publisher's note: Springer Nature remains neutral with regard to jurisdictional claims in published maps and institutional affiliations.